Directed assembly of layered perovskite heterostructures as single crystals

Michael L. Aubrey,[1,7] Abraham Saldivar Valdes,[1,7] Marina R. Filip,[3,4,5] Bridget A. Connor,[1] Kurt P. Lindquist,[1] Jeffrey B. Neaton,[4,5,6] and Hemamala I. Karunadasa*,[1,2]

[1]Department of Chemistry, Stanford University, Stanford, California 94305, United States
[2]Stanford Institute for Materials and Energy Sciences, SLAC National Accelerator Laboratory, Menlo Park, California 94025, United States
[3]Department of Physics, University of Oxford, Oxford OX1 3PU, United Kingdom
[4]Department of Physics, University of California Berkeley, Berkeley, California 94720, United States
[5]Materials Sciences Division, Lawrence Berkeley National Laboratory, Berkeley, California 94720, United States
[6]Kavli Energy NanoSciences Institute at Berkeley, Berkeley, California 94720, United States
[7]These authors contributed equally: Michael L. Aubrey and Abraham Saldivar Valdes
*email: hemamala@stanford.edu

The precise stacking of different 2D structures like graphene and MoS_2 has reinvigorated the field of 2D materials, revealing exotic phenomena at their interfaces.[1,2] These unique interfaces are typically constructed using mechanical or deposition-based methods to build a heterostructure one monolayer at a time.[2,3] In contrast, self-assembly is a scalable technique, where complex materials can selectively form in solution.[4–6] Here we show a synthetic strategy for the self-assembly of layered perovskite-nonperovskite heterostructures into large single crystals in aqueous solution. Using bifunctional organic molecules as directing groups, we have isolated six layered heterostructures that form as an interleaving of perovskite slabs with a different inorganic lattice, previously unknown to crystallize with perovskites. In many cases, these intergrown lattices are 2D congeners of canonical inorganic structure-types. These compounds are the first layered perovskite heterostructures formed using organic templates and characterized by single-crystal X-ray diffraction. Notably, this interleaving of inorganic structures can markedly transform the band structure. Optical data and first principles calculations show substantive coupling between perovskite and intergrowth layers leads to new electronic transitions distributed across both sublattices. Given the technological promise of halide perovskites,[4] this intuitive synthetic route sets a foundation for the directed synthesis of richly structured complex semiconductors that self-assemble in water.

The bulk syntheses of layered heterostructures almost exclusively employ high-temperature solid-state synthetic techniques from which metal-oxide, -chalcogenide, -phosphide, and -halide based materials can be isolated.[7] These materials form via a process called intergrowth, which is the crystallization of one structure on the face of another. More directed intercalation and ion exchange techniques have been developed in oxide perovskites for the post-synthetic preparation of microcrystalline Bi–O (Aurivillius) and halometallate intergrowths from Ruddlesden-Popper phases.[8,9] However, the discovered structural diversity of these materials is limited and each structure stands as an exceptional example from a confined reaction space.

In contrast, layered organic-inorganic halide perovskites are renowned for their structural tunability and low-temperature syntheses.[4] Layered perovskites with the composition A_2MX_4 (A^{1+} = organic or inorganic ion; M^{2+} = metal ion; X^{1-} = halide) are related to the 3D perovskite structure (AMX_3) by dimensional reduction: the conceptual excising of a portion—often a slice along a crystallographic plane—of a parent crystal structure through the formal addition of an ionic salt (*e.g.,* AX).[10] In layered perovskites, A^{1+} is often an alkylammonium cation that partitions the perovskite sheets by forming an organic bilayer. By tailoring the organic cation's structure, an extensive class of halide perovskites can be predictably synthesized.

We hypothesized that the addition of a secondary functional group to an alkylammonium ion could template the intergrowth of a different, dimensionally reduced structure between the perovskite sheets (**Figure 1**). Recently, a sequential film deposition strategy has been employed to form isostructural intergrowths of organic-inorganic perovskites on a planar surface.[11] For brevity, here we reserve the term *intergrowth* to describe *a recurrent co-crystallization of an extended non-perovskite metal-ligand bond network within a layered perovskite*. Encouraged by a previous report of a zwitterionic amino acid forming a layered perovskite and a molecular copper-carboxylate dimer,[12] we first considered isolating layered perovskites with bifunctional alkylammonium oxyacids: $^{+}$R-COOH ($^{+}$R-COOH = 4-(ammoniomethyl)-benzoic acid; pK_a ~ 4), $^{+}$R-PO_3H_2 ($^{+}$R-PO_3H_2 = 3-(ammoniopropyl)-phosphonic acid; pK_a ~ 2.5), and tauric acid (4-(ammonioethyl)-sulfonic acid; pK_a < 0).

1. Acids in the organic layers. In an aqueous 12-M HCl solution of $CuCl_2$, $^+$R-COOH templates the crystallization of the layered perovskite $(R\text{-}COOH)_2CuCl_4$. The organic bilayer assembles as discrete acid dimers, **Figure 2a**, as previously seen in other layered perovskites.[13] As in other Cu-Cl perovskites, the d^9-Cu centers show a Jahn-Teller distortion, with the elongated axis lying parallel to the perovskite sheets. Similarly, $(R\text{-}PO_3H_2)_2CuCl_4$ also crystallizes as a layered perovskite (**Figure 2b**). However, the additional hydrogen bond donors at the phosphonic acid tail, form a 2D hydrogen bond network between the perovskite sheets (**Extended Data Figure 1**). Although many other phosphonic acid-based hydrogen bond networks are reported, this particular arrangement is, to our knowledge, unique.

Tauric acid is considerably more acidic than both $^+$R-COOH and $^+$R-PO_3H_2, to the extent that even in 12-M HCl, the zwitterion, taurine ($^+H_3N\text{-}(CH_2)_2\text{-}SO_3^-$), persists. Nonetheless, the layered perovskite $(H_3O)_2(taurine)_2CuCl_4$ crystallizes under similar reaction conditions. The crystals are deliquescent and decompose in vacuum and dry atmospheres. Since taurine is charge-neutral, the hydronium (H_3O^+) cation is incorporated to balance the anionic perovskite sheet, affording an unusual case of a crystallographically characterized H_3O^+ (**Figure 2c**). Remarkably, the 2D hydronium-sulfonate hydrogen bond network is very similar to that in the layered structure of hydronium triflate ($CF_3SO_3^-\cdot H_3O^+$) (**Extended Data Figure 2**).[14] However, here the lattice is corrugated in order to match lattice parameters with the perovskite sheets (see **Supplementary Video 1**). Notably, this structure represents the templated intergrowth of a 2D inorganic structure within a perovskite as envisioned in **Figure 1**.

2. Metals in the organic layers. The co-crystallization of a 2D cationic sublattice in $(H_3O)_2(taurine)_2CuCl_4$ through the inclusion of the zwitterion taurine motivated us to search for structures where taurine coordinates to a metal cation in place of hydronium. Since the zwitterionic taurine persists across all aqueous pH values,[15] and a high chloride concentration must be maintained in order to selectively crystallize $CuCl_x$ salts over $Cu(H_2O)_x$ salts, we used concentrated metal chloride solutions in place of HCl.

Solutions of $CuCl_2$ and taurine in 10-M LiCl(*aq*) selectively crystallize $Li_2(taurine)_2CuCl_4$, **Figures 2d and 3c**. Between the perovskite sheets, tetrahedral lithium ions are coordinated to the sulfonate tails within the taurine bilayer. This 2D *templated intergrowth sublattice* is isostructural with the metastable α-$(NH_4)LiSO_4$, **Figure 3b**.[16] Likewise, the intergrowth sublattice and α-$(NH_4)LiSO_4$ are 2D congeners of the parent structure Li_2SO_4, sliced along the (001) plane (**Figure 3a**).[17] Therefore, we envision the single crystal $Li_2(taurine)_2CuCl_4$ as a composite lattice of dimensionally reduced analogues of the parent ternaries Li_2SO_4 and perovskite. Note that a directly analogous $ACuCl_3$ 3D perovskite remains unknown.

The commensurate co-crystallization of the perovskite and lithium sulfonate sheets necessitates that both structures occupy a shared unit cell. Using α-$(NH_4)LiSO_4$ and $(C_3H_7NH_3)_2CuCl_4$ as reference structures,[18,19] the lattice strain required to form such a heterostructure can be approximated for each 2D sublattice (**Extended Data Tables 1–4**). From this analysis, we can quantify the degree to which each sublattice distorts to form an atom-perfect heterointerface in a manner analogous to lattice mismatch parameters often reported for interfaces formed by deposition-based heteroepitaxy.[3] However, because single-crystal X-ray diffraction affords 3D atomic coordinates and unit cell dimensions, we can calculate a 3D strain tensor for the primitive cell of each sublattice and visualize a trajectory through which the lattice distorts by animating atom displacements.

The relative strain found for the sulfonate slab is accommodated by a slight dihedral rotation along the 1D Li-O chains of vertex-sharing tetrahedra (see **Supplementary Video 2**). The 3.8% areal expansion of the lithium sulfonate slab (**Extended Data Table 1**) is complementary to the 5.7% contraction of the perovskite slab and, is mostly accounted for by distortion along a single axis. In the nearly isostructural $Li_2(taurine)_2MnCl_4$, we observe a smaller but similar distortion, without the Jahn-Teller distortion of the Cu^{2+} analog (**Supplementary Video 3**).

Using 5-M $MgCl_2$(*aq*) in place of 10-M LiCl(*aq*), an extended magnesium sulfonate forms as the intergrowth in $(Mg(H_2O)_2)(taurine)_2CuCl_4$, **Figure 3c**. The magnesium sulfonate hydrate slab is essentially isostructural to that in $KMg(H_{0.5}SO_4)_2\cdot 2H_2O$ (**Figure 3b**), which in turn can be derived from 3D $MgSO_4$ sliced along the (001) plane (**Figure 3a**).[20,21] This intergrowth sublattice features 1D chains of sulfonate-bridged, $Mg(H_2O)_2^{2+}$ ions hydrogen bonded to neighboring chains to form a 2D network (**Extended Data Figure 3**). In comparison to $KMg(H_{0.5}SO_4)_2\cdot 2H_2O$, the magnesium sulfonate sublattice displays an in-plane expansion of 4.1%, and a dramatic elongation of the magnesium sulfonate chains of 11%. This is largely accommodated for by tilting the bridging sulfonates as illustrated in the **Supplementary Video 4**.

3. Intergrowths in double perovskites. The structural diversity of halide double perovskites,[22] where an ordered combination of two different metal cations occupy the octahedral sites, can also be expanded by templating intergrowths. We found that the phenethylammonium cation (PEA^+) templates the layered double perovskite $(PEA)_4Cu^{I}In^{III}Cl_8$, where the metals in the $CuInCl_8^{4-}$ slabs form an ordered checkerboard. Replacing PEA^+ with the histammonium dication (HIS^{2+}), under similar reaction conditions as for $(PEA)_4CuInCl_8$, affords the heterostructure $(CuCl_2)_4(HIS)_4CuInCl_8$ after several recrystallizations. In this structure, the same $CuInCl_8^{4-}$ sublattice is templated by the ethylammonium head of HIS^{2+} (**Figure 1**) while $(CuCl_2)_n^-$ chains of edge-sharing tetrahedra are templated by the imidazolium tail, **Extended Data Figure 4**. Although copper(I) halides are known for their structural diversity,[23] the chain structure in $(CuCl_2)_4(HIS)_4CuInCl_8$ is rare.[24] Relative to an isostructural chain found in a phthalazinium salt, the intergrowth chain displays a linear contraction of 1.3% while the double perovskite slab contracts in plane by 4.7% relative to $(PEA)_4CuInCl_8$, see **Supplementary Video 5**.

4. Heterostructures of perovskite and PbX_2 (X = Cl, Br). While taurine and HIS^{2+} both template perovskite intergrowths, the layers are well-separated, with weak electronic interactions

between the perovskite and intergrowth sublattices. Seeking to reduce the distances between layers and incorporate softer metal-ligand interactions into the intergrowth we considered the smaller zwitterion cysteamine ($^{+}NH_3(CH_2)_2S^{-}$; CYS).

Single crystals of the heterostructure $(Pb_2Cl_2)(CYS)_2PbCl_4$, featuring a lead-chloride intergrowth, were isolated from a solution of lead salts and CYS in 6-M NaCl(*aq*). A subtle ordering of the CYS zwitterion affords two crystallographically distinct perovskite sublattices with an ABA′B stacking sequence (**Figure 4b**) where A and A′ are statistically disordered in about 1 of every 14 repeat units. Notably, the intergrowth is bonded to the perovskite slabs through a bridging chloride, resulting in a 3D lead-chloride network. The intergrowth sublattice can be derived from a slice cut along the (001) plane of 3D $PbCl_2$ (**Extended Data Figures 5 & 6**),[25] although such layered analogues of PbX_2 have not been isolated elsewhere. The intergrowth displays an in-plane contraction of 5.2%, relative to $PbCl_2$,[25] accompanying a complementary 6.0% expansion of the perovskite sublattice relative to $(propylammonium)_2PbCl_4$ (**Supplementary Videos 6 and 7**).[26]

The heterostructure $(PbBr_2)_2(AMTP)_2PbBr_4$ ($AMTP^{+}$ = 4-ammoniomethyl-tetrahydropyran) is similar to $(Pb_2Cl_2)(CYS)_2PbCl_4$, containing a $PbBr_2$ intergrowth that is isostructural to 3D $PbBr_2$ sliced along the (001) plane **Extended Data Figure 5 & 6**. But here, the $AMTP^{+}$ charge balances the perovskite slab and a charge-neutral $PbBr_2$ intergrowth is templated by the tetrahydropyran tails, **Figure 4a**. In contrast to $(Pb_2Cl_2)(CYS)_2PbCl_4$, the perovskite and intergrowth sheets are separated by the insulating organic cations. The areal strain of the perovskite sheet is comparable to those in other intergrowths (3.1%, contraction). However, the relative strain of the $PbBr_2$(tetrahydropyran) slab compared to $PbBr_2$ is large, 14% contraction,[25] originating from the formal substitution of terminal bromides in the $PbBr_2$ with smaller tetrahydropyran capping ligands in the intergrowth (see **Supplementary Videos 8 and 9**).

5. Electronic structures of the perovskite-PbX_2 intergrowths. The structural similarities between $(Pb_2Cl_2)(CYS)_2PbCl_4$ and $(PbBr_2)_2(AMTP)_2PbBr_4$ present a unique opportunity to explore how the interactions between the perovskite sheets and the PbX_2-like intergrowths impact their bulk electronic structures. Importantly, in the Pb–Cl structure the intergrowth is directly connected to the perovskite layer via the apical chloride of the perovskite sheet, whereas the intergrowth and perovskite layer are well separated by the organic layer in the Pb–Br structure.

For $(PbBr_2)_2(AMTP)_2PbBr_4$, our density functional theory (DFT) calculations reveal a band structure (**Figure 4c**) that is similar to those of typical 2D lead-halide perovskites,[27] with a direct gap between the conduction and valence band extrema, which are exclusively composed of electronic states within the perovskite sublattice. Consistent with this, the optical properties of $(PbBr_2)_2(AMTP)_2PbBr_4$ are like those of typical Pb–Br perovskites.[28]

The low-temperature UV-*vis* diffuse reflectance spectrum and thin-film transmission spectrum for $(PbBr_2)_2(AMTP)_2PbBr_4$ are shown in **Figure 4e** (plotted as pseudo-absorbance and absorbance plots, respectively; see Methods). The spectra show an excitonic absorption (from a bound electron-hole pair) at ca. 3.1 eV, which is separated from the onset of the continuum. These spectra are very similar to thin-film or powder spectra of the 2D perovskite $(butylammonium)_2PbBr_4$. As is the case for $(PbBr_2)_2(AMTP)_2PbBr_4$, the excitonic absorbance in 2D perovskites is more pronounced in transmission spectra of oriented films, although it is evident in reflectance spectra of dilute powders as well (**Supplementary Figures S9–S10**). Powders of $(PbBr_2)_2(AMTP)_2PbBr_4$ also display narrow blue (ca. 3.05 eV) excitonic photoluminescence at room temperature, as seen in most layered Pb–Br perovskites (**Supplementary Figure S13**).[28]

Optical absorption spectra calculated using first principles many-body perturbation theory within the GW approximation[29] and the Bethe-Salpeter Equation (GW+BSE)[30–32] are in good qualitative agreement with the measured spectra. The real-space representation of the square modulus of the exciton wave function—corresponding to the first excited state—reveals an expected localization of the bound electron-hole pair within the perovskite layer (see **Figure 4g** and Methods).

The band structure for a simplified model structure of $(Pb_2Cl_2)(CYS)_2PbCl_4$ (described in Methods; see **Extended Data Figure 7**) shows state mixing between the intergrowth and the perovskite layers, due to the bridging chloride connecting the two layers. The bottom of the conduction band corresponds predominantly to states localized on the Pb^{2+} ions of the perovskite sublattice. Unlike $(PbBr_2)_2(AMTP)_2PbBr_4$, the top of the valence band is primarily composed of states from the intergrowth sublattice, with more than 50% of the valence band top's composition attributed to the sulfur ions of the intergrowth layer. The intergrowth layer not only contributes directly to the shape and character of the valence band, but also indirectly to the dispersion of the conduction band, by inducing a strain in the perovskite lattice leading to a slightly indirect bandgap, ca. 70 meV lower than the direct gap at Γ.

Interestingly, the intergrowth changes the optical properties and charge distribution in $(Pb_2Cl_2)(CYS)_2PbCl_4$ compared to those of typical 2D Pb–Cl perovskites.[28] Layered Pb–Cl perovskite films typically show a sharp excitonic absorption peak around 3.81(7) eV at room temperature (averaging data from 10 perovskites; **Supplementary Figure S11-S12**). In contrast, the room-temperature absorption spectrum of $(Pb_2Cl_2)(CYS)_2PbCl_4$ powder shows a significantly broadened absorption onset starting from ca. 3.0 eV with a plateau between 3.6 and 3.8 eV (**Supplementary Figure S9)**. Likely due to the 3D Pb–Cl connectivity, $(Pb_2Cl_2)(CYS)_2PbCl_4$ does not readily form films. Photoluminescence spectroscopy at 80 K also reveals a broad, low-energy emission centered at 1.85 eV with a very large Stokes shift of about 1.8 eV (**Supplementary Figure S14**).

GW+BSE calculations performed on the ordered structural model of $(Pb_2Cl_2)(CYS)_2PbCl_4$ predict a well-defined direct exciton at the onset of the optical spectrum (**Figure 4f**). Notably, this computed peak corresponds to a delocalized excitonic state, which extends across both the intergrowth and perovskite layers (**Figure 4h**), consistent with the relative orbital contributions of the valence band maximum and conduction band minimum. The

experimental spectrum displays a more complex structure of this feature, comprising several closely spaced peaks (**Figure 4f**). These additional peaks may arise from indirect (phonon-assisted) excitons as well as from the presence of crystallographically unique perovskite sublattices and stacking faults that pervade the material, which are not accounted for in the calculated spectrum.

Further investigations are required to fully understand and exploit the nature of optical excitation and emission in these elaborate heterostructures, including probing the potential of observing and manipulating interlayer excitons, like those recently found in heterobilayers of transition-metal dichalcogenides.[33] However, it is clear that both the electronic and optical properties of halide perovskites can be directly engineered through the templating of single-crystal intergrowths. Thus, apart from the potential for realizing different properties in the distinct inorganic layers these heterostructures can also exhibit emergent properties not seen in the parent 2D materials.

REFERENCES

1. Hwang, H. Y., Iwasa, Y., Kawasaki, M., Keimer, B., Nagaosa, N. & Tokura, Y. Emergent phenomena at oxide interfaces. *Nat. Mater.* **11,** 103–113 (2012).
2. Novoselov, K. S., Mishchenko, A., Carvalho, A. & Neto, A. H. C. 2D materials and van der Waals heterostructures. *Science* **353,** aac9439-13 (2016).
3. Wong, F. J. & Ramanathan, S. Nonisostructural complex oxide heteroepitaxy. *J. Vac. Sci. Technol. A* **32,** 040801–17 (2014).
4. Saparov, B. & Mitzi, D. B. Organic–inorganic perovskites: structural versatility for functional materials design. *Chem. Rev.* **116,** 4558–4596 (2016).
5. Li, J., Chen, Z., Wang, R.-J. & Proserpio, D. M. Low temperature route towards new materials: solvothermal synthesis of metal chalcogenides in ethylenediamine. *Coord. Chem. Rev.* **190,** 707–735 (1999).
6. Lobo, R. F., Zones, S. I. & Davis, M. E. Structure-direction in zeolite synthesis. *J. Incl. Phenom. Mol. Recognit. Chem.* **21,** 47–78 (1995).
7. Rao, C. N. R. & Thomas, J. M. Intergrowth structures: the chemistry of solid-solid interfaces. *Acc. Chem. Res.* **18,** 113–119 (2002).
8. Schaak, R. E. & Mallouk, T. E. Perovskites by design: a toolbox of solid-state reactions. *Chem. Mater.* **14,** 1455–1471 (2002).
9. Viciu, L., Koenig, J., Spinu, L., Zhou, W. L. & Wiley, J. B. Insertion of a two-dimensional iron-chloride network between perovskite blocks. Synthesis and characterization of the layered oxyhalide, (FeCl)$LaNb_2O_7$. *Chem. Mater.* **15,** 1480–1485 (2003).
10. Tulsky, E. G. & Long, J. R. Dimensional reduction: a practical formalism for manipulating solid structures. *Chem. Mater.* **13,** 1149–1166 (2001).
11. Shi, E., Yuan, B., Shiring, S. B., Gao, Y., Akriti, Guo, Y., Su, C., Lai, M., Yang, P., Kong, J., Savoie, B. M., Yu, Y. & Dou, L. Two-dimensional halide perovskite lateral epitaxial heterostructures. *Nature* **580,** 614–620 (2020).
12. Mercier, N. & Riou, A. An organic–inorganic hybrid perovskite containing copper paddle-wheel clusters linking perovskite layers: $[Cu(O_2C–(CH_2)_3–NH_3)_2]PbBr_4$. *Chem. Commun.* **123,** 844–845 (2004).
13. AlShammari, M. B., Kaiba, A., Guionneau, P., Geesi, M. H., Aljohani, T. & Riadi, Y. Phase transitions, optical and electronic properties of the layered perovskite hybrid $[NH_3(CH_2)_2COOH]_2CdCl_4$ of γ-aminobutyric acid (GABA). *Chem. Phys. Lett.* **702,** 8–15 (2018).
14. Spencer, J. B. & Lundgren, J.-O. Hydrogen bond studies. LXXIII.* The crystal structure of trifluoromethanesulphonic acid monohydrate, $H_3O^+CF_3SO_3^-$, at 298 and 83°K. **B29,** 1923–1928 (1973).
15. King, E. J. The ionization constants of taurine and its activity coefficient in hydrochloric acid solutions from electromotive force measurements. *J. Am. Chem. Soc.* **75,** 2204–2209 (1953).
16. Pietraszko, A. & Lukaszewicz, K. Crystal structure of α-$LiNH_4SO_4$ in the basic polytypic modification. *Pol. J. Chem.* **66,** 2057–2061 (1992).
17. Nord, A. G. Crystal structure of β-Li_2SO_4. *Acta Crystallogr. B* **32,** 982–983 (1976).
18. Doudin, B. & Chapuis, G. Structure analysis of the high-temperature phases of $[NH_3(C_3H_7)]_2CuCl_4$. I. The commensurate phases. *Acta Crystallogr. B* **46,** 175–180 (1990).
19. Komornicka, D., Wołcyrz, M. & Pietraszko, A. olymorphism and polytypism of α-$LiNH_4SO_4$ crystals. Monte Carlo modeling based on X-ray diffuse scattering. *Cryst. Growth Des.* **14,** 5784–5793 (2014).
20. Macíček, J., Gradinarov, S., Bontchev, R. & Balarew, C. A short dynamically symmetrical hydrogen bond in the structure of $K[Mg(H_{0.5}SO_4)_2(H_2O)_2]$. *Acta Crystallogr. C* **50,** 1185–1188 (1994).
21. Rentzeperis, P. J. & Soldatos, C. T. The crystal structure of the anhydrous magnesium sulphate. *Acta Crystallogr.* **11,** 686–688 (1958).
22. Wolf, N. R., Connor, B. A., Slavney, A. H. & Karunadasa, H. Doubling the stakes: the promise of halide double perovskites. *Angew. Chem. Int. Ed.* anie.202016185 (2021). doi:10.1002/anie.202016185
23. Subramanian, L. & Hoffmann, R. Bonding in halocuprates. *Inorg. Chem.* **31,** 1021–1029 (1992).
24. Plasseraud, L., Cattey, H. & Richard, P. Isolation and X-ray characterization of $\{[phthalazinium](CuCl_2)\}_\infty$: a new example of a dichlorocuprate(I) presenting a rare staircase chain structure. *Z. Naturforschung B* **65,** 317–322
25. Lumbreras, M. Structure and ionic conductivity of mixed lead halides $PbCl_{2x}Br_{2(1-x)}$. II. *Solid State Ion.* **20,** 295–304 (1986).
26. Meresse, A. & Daoud, A. Bis(*n*-propylammonium) tetrachloroplumbate. *Acta Crystallogr. C* **45,** 194–196 (1989).
27. Kamminga, M. E.; Fang, H.-H.; Filip, M. R.; Giustino, F.; Baas, J.; Blake, G. R.; Loi, M. A.; Palstra, T. T. M. Confinement effects in low-dimensional lead iodide perovskite hybrids. *Chem. Mater.* **2016**, *28* (13), 4554–4562.
28. Smith, M. D., Connor, B. A. & Karunadasa, H. I. Tuning the luminescence of layered halide perovskites. *Chem. Rev.* **119,** 3104–3139 (2019).
29. Hybertsen, M. S. & Louie, S. G. Electron correlation in semiconductors and insulators: band gaps and quasiparticle energies. *Phys. Rev. B* **34,** 5390–5413 (1986).
30. Rohlfing, M. & Louie, S. G. Electron-hole excitations in semiconductors and insulators. *Phys. Rev. Lett.* **81,** 2312–2315 (1998).
31. Rohlfing, M. & Louie, S. G. Electron-hole excitations and optical spectra from first principles. *Phys. Rev. B* **62,** 4927–4944 (2000).

32. Strinati, G. Application of the Green's functions method to the study of the optical properties of semiconductors. *Riv. Nuovo Cimento* **11,** 1–86 (1988).
33. Rivera, P., Yu, H., Seyler, K. L., Wilson, N. P., Yao, W. & Xu, X. Interlayer valley excitons in heterobilayers of transition metal dichalcogenides. *Nat. Nanotechnol.* **13,** 1004–1015 (2018).

FIGURE CAPTIONS

Figure 1| Reaction design scheme for targeting templated perovskite intergrowths. Illustrations of the perovskite lattices are shown in light blue and a hypothetical, lattice-matched structure in green. Templating groups (inset) for the perovskite and intergrowth structures are represented as blue and yellow circles, respectively.

Figure 2| Oxyacids in the organic layers of perovskites and the exchange of H_3O^+ with Li^+. Single-crystal structures of layered Cu−Cl perovskites with alkylammonium-oxyacid organic templates: (a) $(RCOOH)_2CuCl_4$; (b) $(RPO(OH)_2)_2CuCl_4$ and (c) $(H_3O)_2(taurine)_2CuCl_4$. (d) Single-crystal structure of $Li_2(taurine)_2CuCl_4$, which is related to that of $(H_3O)_2(taurine)_2CuCl_4$ by a conceptual ion exchange of H_3O^+ for Li^+ (insets). Teal, light-green, grey, blue, white, red, yellow, pink, and light-blue spheres represent Cu, Cl, C, N, H, O, S, P, and Li atoms, respectively.

Figure 3| Conceptualized dimensional reduction of 3D parent structures to afford the layered heterostructures. The addition of an alkylammonium salt, a sulfate salt, or a water affords layered derivatives (b) of the parent 3D structures (a). Note, the parent perovskite $RbCuCl_3$ is unknown, but $RbCuF_3$ is known. The inclusion of two functional groups (alkylammonium and alkylsulfonate) in a single molecule directs the formation of the single-crystal heterostructures (c). Li, Cu, Mg, Rb, K, Cl, S, O, C, N, and H atoms are shown as light blue, teal, green, light-grey, pink, lime-green, yellow, red, dark-grey, blue, and white spheres, respectively. The disordered Jahn-Teller distortion of the $CuCl_4$ polyhedra in $Li_2(taurine)_2CuCl_4$ and $(Mg(H_2O)_2)(taurine)_2CuCl_4$ is not depicted for clarity.

Figure 4| Comparison of the Pb–X perovskite-PbX_2 (X = Cl, Br) heterostructures. Single-crystal X-ray diffraction structures of a) $(PbBr_2)_2(AMTP)_2PbBr_4$ and b) $(Pb_2Cl_2)(CYS)_2PbCl_4$. Insets show coordination of $AMTP^+$ and CYS to the intergrowths. Pb, Cl, Br, S, C, O, and N atoms are shown as light blue, lime-green, orange, yellow, grey, red, and blue spheres, respectively. Perovskite and PbX_2-like sublattices are shaded in light blue and yellow, respectively. Hydrogen atoms are omitted for clarity. DFT-PBE band structures of c) $(PbBr_2)_2(AMTP)_2PbBr_4$ and d) $(Pb_2Cl_2)(CYS)_2PbCl_4$ with orbital contributions from the perovskite and intergrowth sublattices shown in blue and yellow, respectively. Experimental (grey lines) and calculated absorption spectra with (GW-BSE, red line) and without (GW, red dashed line) electron-hole interactions for e) $(PbBr_2)_2(AMTP)_2PbBr_4$ and f) $(Pb_2Cl_2)(CYS)_2PbCl_4$. All calculated spectra are offset by +0.55 eV, to match the experimental onsets. Isosurfaces representing the spatial distribution of the lowest-lying optically active exciton for $(PbBr_2)_2(AMTP)_2PbBr_4$ (g) and $(Pb_2Cl_2)(CYS)_2PbCl_4$ (h), see Methods for details.

METHODS

General Procedures and Methods. All reagent grade chemicals were acquired from commercial suppliers and used without further purification. Air-free syntheses and handling of air-sensitive materials were performed either in a nitrogen-filled glovebox or using standard Schlenk techniques. Solvents were column dried and degassed using a J.C. Meyer solvent system prior to use with air-sensitive compounds.

Relative lattice strain estimations. Sublattice strain tensors for both the perovskite and the intergrowth sheets in the single-crystal structures were determined relative to previously reported structures of the parent sublattices in simple layered compounds. The parent layered materials used as references were selected based on the structural similarity of the organic structures to the templating organic ammoniums in the intergrowths reported here (Extended Data Table 1). For each perovskite sublattice a primitive cell was constructed using symmetry equivalent terminal halides of the perovskite slab as lattice points. For each intergrowth, lattice points were selected as to include all the atoms in the parent sublattice (see Supplementary Videos). Engineering strain tensors were calculated using the derived primitive cells and the online software suite ISOTROPY and component program ISODISTORT.[34,35] Relative linear, areal, and volumetric strains were calculated from the strain tensor, ε, in Equation 1 as

$$\varepsilon = \begin{bmatrix} \varepsilon_{aa} & \frac{\gamma_{ab}}{2} & \frac{\gamma_{ac}}{2} \\ \frac{\gamma_{ab}}{2} & \varepsilon_{bb} & \frac{\gamma_{bc}}{2} \\ \frac{\gamma_{ac}}{2} & \frac{\gamma_{bc}}{2} & \varepsilon_{cc} \end{bmatrix} \quad (1)$$

Where *a*, *b,* and *c* correspond to the axes of the primitive cell, and γ_{ab}, γ_{ac}, and γ_{bc} are the respective engineering shear strains. The fractional change in dimension is reported as $|\varepsilon+I|$ for the corresponding submatrix where I is the identity matrix. These results are summarized in **Extended Data Tables 1–4**.

Chemical structures are fundamentally discrete, therefore we find the most apt comparisons are those between the most similar structures available, as reported here. While the best possible structural comparisons are made using the most similar chemical structures available, the observed distribution of lattice parameters found in the halide perovskites may provide valuable insight as well. Surveying the Cambridge Structural Database, we note relative standard deviations from the average are <1.6% for perovskite lattice parameters (collated as the B-X-B distances where B is the octahedral cation) in perovskite and layered perovskite structures with different A-sites for the compositions A-Cu-Cl, A-Mn-Cl, A-Pb-Cl, and A-Pb-Br.

Animations of the relative atomic displacements between the observed sublattices in the heterostructures and their respective reference compounds (see **Extended Data Table 1**) were constructed by extracting an equivalent portion of each sublattice into a Cartesian coordinate system using the software suite Diamond 4.6 (Crystal Impact GbR). The two structures were overlaid and difference vectors were calculated for each equivalent atom pair. Intermediate frames were calculated by adding a linearly scaled fraction of the difference vector to the initial positions of the atoms in the reference parent structures. Each resulting animation illustrates the distortion from the reference compound to the sublattice found in the intergrowth. See **Supplementary Videos**.

Coordination number and bond valence sums. Bond valence sums were determined for the purpose of consistently assigning the coordination number about each lead center in $PbCl_2$, $PbBr_2$, $(Pb_2Cl_2)_2(CYS)_2PbCl_4$, and $(PbBr_2)_2(AMPT)PbBr_4$. This was calculated using the software packages ToposPro 5.4 and the component program AutoCN, which determines the adjacency matrix, coordination numbers, contact classifications, and bond valence sums.[25,36] For all calculations, Slater's radius[37] of 1.80 Å was used for lead. By this method the accepted coordination assignments for $PbBr_2$ and $PbCl_2$ of [7+2] were determined.[38]

Single-Crystal X-ray Diffraction. Crystals were coated with N-Paratone oil, mounted on a Kapton® loop, and transferred to a Bruker D8 diffractometer. Frames were collected using ω and ψ scans. The radiation source was Mo Kα-radiation (λ = 0.71073 Å) for all samples except those that follow. For the compound $H_3O(taurine)CuCl_4$ the radiation source was the synchrotron at the Advanced Light Source (ALS) (λ = 0.72880 Å) on beamline 12.2.1. Single-crystal diffraction data for the compound $(PbBr_2)_2(AMTP)_2PbBr_4$ were collected at the ALS (beamline 11.3.1, λ = 0.7749 Å).

Frames were integrated and corrected for Lorentz and polarization effects using SAINT V8.38A and were corrected for absorption effects using SADABS V2012.[39] Space-group assignments were based upon systematic absences, *E*-statistics, agreement factors for equivalent reflections, and successful refinement of the structure. The structures were solved by direct methods, expanded through successive difference Fourier maps using SHELXT,[40] and refined against all data using the SHELXL-2014[41] software package as implemented in Olex2.[42] Weighted *R* factors, R_W, and all goodness-of-fit indicators are based on F^2. Summary diffraction and refinement statistics can be found in Supplementary Tables S1 and S2.

Powder X-ray Diffraction. Bulk powder samples were ground with a mortar and pestle and staged on a Bruker D8 advance diffractometer in a Bragg-Brentano θ–θ geometry. Diffraction patterns were collected between the 2θ angles of 5º and 60º using a Cu-Kα radiation source. The resulting patterns were matched to their corresponding unit cells determined by single-crystal X-ray diffraction using structureless Le Bail whole pattern fitting as implemented in the software package GSAS-II.[43] Summary diffraction and refinement statistics can be found in Supplementary Tables S3 and S4.

Diffuse Reflectance Measurements. Samples for room-temperature diffuse reflectance measurements were collected using a Shimadzu-2600 UV-*vis*-NIR spectrophotometer with a $BaSO_4$ coated integrating sphere (Shimadzu ISR-2600). Sample reflectance was measured relative to $BaSO_4$ and samples were prepared by dilution of the sample to 2-5 wt% in a $BaSO_4$ powder mull.

Low-temperature diffuse reflectance measurements were collected using a Janis ST-100 helium-cooled cryostat outfitted with a temperature controller and fused quartz windows. Powder mulls of samples (1-3 wt%) in $BaSO_4$ were dispersed in a minimal volume of a solution of 1 wt% polymethylmethacrylate in toluene and drop-cast onto a copper sample mount attached to the cold head and aligned approximately parallel to the quartz window. The cryostat was mounted inside of an Agilent Cary-6000 UV-*vis*-NIR spectrophotometer equipped with Agilent's Universal Measurement Apparatus (UMA) that enables the measurement of reflectance spectra with independent control of the angles of incidence and reflectance at the sample. All samples were sufficiently micronized and milled into a large excess of $BaSO_4$ such that qualitatively no angular dependance of the reflectance spectra was observed. Reflectance spectra were converted to pseudo-absorbance spectra using the Kubelka-Munk equation.

Thin film UV-*vis* absorption spectroscopy. Thin film samples deposited on quartz glass substrates were attached to the cold head of a liquid helium cooled cryostat with a sample chamber equipped with quartz glass windows mounted in a Cary 500 UV-*vis*-NIR spectrophotometer and transmission spectra were collected. In order to compare transmission spectra to diffuse reflectance spectra, the data were converted to absorbance units.

Simplified structural model of $(Pb_2Cl_2)(CYS)_2PbCl_4$. Our best refinement of the single crystal X-ray diffraction data yielded 1) an orthorhombic crystal lattice with unit cell sizes 53.51 Å, 8.81 Å and 7.49 Å, consisting of 248 atoms in the unit cell, and 2) disordered occupation

of sites of the intergrowth lattice, alternating between two different possible sites with occupation numbers of approximately 0.93 and 0.07, respectively. To obtain a structure amenable for electronic structure calculations, we constructed a simplified model for $Pb_2Cl_2)_2(CYS)_2PbCl_4$ using two approximations. Firstly, we observed that structural ordering that leads to the two unique perovskite slabs is subtle with very little difference in chemical bonding between the A and A′ slabs in **Figure 4b**. Using the software package VESTA,[44] we reduced the length of the *a*-axis by half, effectively removing an *a*-glide $\perp$ *b* from the structure (**Extended Data Figure 7**), and reduced the crystal symmetry of the unit cell to P1. Secondly, we fixed the Pb, S, and Cl ions in the intergrowth to the majority occupation sites. While halving the unit cell size along the *a* direction is not expected to affect the electronic structure of the system significantly, the disordered occupation of the intergrowth sites may have an impact on the shape of the valence band top. This disorder, along with indirect (phonon-assisted) excitons, may contribute to the multiple closely spaced peaks seen in the experimental optical spectrum, both of which are not captured in the calculated spectrum.

Electronic structure calculations. Density functional theory (DFT)[45] calculations were performed within the generalized gradient approximation in the Perdew-Burke-Ernzerhof parametrization (PBE),[46] including spin-orbit coupling, as implemented in the Quantum Espresso package,[47,48] and using the experimental lattice parameters determined in this work and relaxed atomic positions (see *Simplified structure model of $(Pb_2Cl_2)(CYS)_2PbCl_4$* and Extended Data Figure 7), using a 1×3×3 *k*-point grid. $(Pb_2Cl_2)(CYS)_2PbCl_4$ includes 124 atoms and 544 electrons in the unit cell, while $(PbBr_2)_2(AMPT)_2PbBr_4$ includes 110 atoms and 392 electrons in the unit cell. For all elements we used norm-conserving pseudopotentials as available on the Pseudo-Dojo library,[49] and a plane wave cutoff of 50 Ry. For both structures we calculate the total energy and charge density using a Γ-centered *k*-point grid of 1×3×3.

We calculate the quasiparticle corrections to the DFT Kohn-Sham eigenvalues of both structures within the single-shot G_0W_0 approximation, including spin-orbit coupling, as implemented in the BerkeleyGW code.[50–52] For both structures we calculate the dielectric function (and self-energy) using a half-shifted (Γ-centered) 1×4×4 *k*-grid, and 400 empty states, amounting to a total of 944 and 792 bands for $(Pb_2Cl_2)(CYS)_2PbCl_4$, and $(PbBr_2)_2(AMPT)_2PbBr_4$, respectively. Based on convergence tests performed on model Ruddlesden-Popper perovskites, we expect this computational setup to yield band gaps that are underestimated with respect to the converged quasiparticle band gap by at least 0.2 eV, a compromise we make to reduce the significant computational effort for GW+BSE calculations on these large systems. We find direct quasiparticle band gaps at the Γ-point of 3.3 eV and 2.9 eV for $(Pb_2Cl_2)(CYS)_2PbCl_4$, and $(PbBr_2)_2(AMPT)_2PbBr_4$, respectively, both values underestimated with respect to the optical absorption onsets observed from experiment.

We calculate the optical absorption spectrum building on our single shot GW calculations via the Bethe-Salpeter equation approach, also using the BerkeleyGW code. In our BSE calculations, we calculate the electron-hole kernel on a 1×4×4 coarse *k*-point grid using 46 and 24 conduction and valence band states for $(Pb_2Cl_2)(CYS)_2PbCl_4$, and $(PbBr_2)_2(AMPT)_2PbBr_4$, respectively. We interpolate the quasiparticle eigenvalues and electron-hole kernel onto a Γ-centered fine grid of 1×10×10 and 1×20×20 for $(Pb_2Cl_2)(CYS)_2PbCl_4$, and $(PbBr_2)_2(AMPT)PbBr_4$, respectively and including 44 conduction and valence states and 20 conduction and valence states for $(Pb_2Cl_2)(CYS)_2PbCl_4$, and $(PbBr_2)_2(AMPT)_2PbBr_4$, respectively. This computational setup yields a converged optical absorption spectrum in the energy range shown in **Figure 4**, and exciton binding energies with an error-bar of approximately 60 meV. We calculate exciton binding energies of 366 meV and 358 meV for $(Pb_2Cl_2)(CYS)_2PbCl_4$ and $(PbBr_2)_2(AMPT)_2PbBr_4$, respectively. Exciton conditional probability distributions depicted in **Figures 4 g–h** are calculated by summing up square moduli of the exciton wave functions' distributions calculated from GW+BSE with the hole fixed at different positions, as follows. For $(PbBr_2)_2(AMPT)_2PbBr_4$ we fix the hole on two different positions corresponding to neighboring apical and equatorial bromine of one of the two perovskite layers in the unit cell, and for $(Pb_2Cl_2)_2(CYS)_2PbCl_4$ we fixed the holes on the four different positions corresponding to sulfur ions in one of the two intergrowth layers of the unit cell. These choices were informed by the majority chemical composition of the valence band top at the Γ-point.

Synthesis of $(RCOOH)_2CuCl_4$ ($RCOOH^+$ = 4-(ammoniomethyl)benzoic acid). The reagents $CuCl_2$ (19 mg, 0.14 mmol) and 4-(aminomethyl)benzoic acid (44 mg, 0.29 mmol) were added to a 4-mL glass vial and dissolved in 0.5 mL of 12-M HCl (*aq*). The solution was heated at 100 °C for 6 h then slowly cooled to room temperature to yield the crystalline product as large yellow plates. *Elemental Analysis*. Calculated: C 37.70%, H 3.95%, N 5.49%. Found: C 37.91%, H 3.96%, N 5.70%.

Synthesis of $(RPO(OH)_2)_2CuCl_4$ ($RPO(OH)_2^+$ = 3-(ammoniopropyl)phosphonic acid). The reagents $CuCl_2$ (19 mg, 0.14 mmol) and 3-(aminopropyl)phosphonic acid (40 mg, 0.29 mmol) were added to a 4-mL glass vial and dissolved in 0.1 mL of 6-M HCl (*aq*). The vial was heated to 100 °C for 6 h then slowly cooled to room temperature to yield the product as large yellow plate-shaped crystals. *Elemental Analysis*. Calculated: C 14.84%, H 4.57%, N 5.77%. Found: C 14.97%, H 4.65%, N 5.83%.

Synthesis of $(H_3O)_2(taurine)_2CuCl_4$ (taurine = $^+H_3N(CH_2)_2SO_3^-$). Taurine (2-aminoethanesulfonic acid; 75 mg, 0.60 mmol) and anhydrous $CuCl_2$ (40 mg, 0.30 mmol) were dissolved in 0.3 mL of concentrated hydrochloric acid in a 4-mL vial. The mixture was heated to 100 °C (Caution: be aware of pressure build-up) until the solids dissolved and the vial was left to cool over the course of 2–3 h to yield brown plate-like crystals. The product was unstable outside of the mother liquor. Crystals selected for single-crystal diffraction were quickly immersed in N-Paratone oil and transferred to a cold N_2 stream to avoid decomposition.

Synthesis of $Li_2(taurine)_2CuCl_4$. Taurine (75 mg, 0.60 mmol) and anhydrous $CuCl_2$ (0.30 mmol) were added to 0.3 mL of a 10 M solution of aqueous LiCl in a 4-mL vial. The mixture was heated to 100 °C and stirred until the precursors were completely dissolved. Then, the vial was left to cool for 2 - 3 h and square yellow plate-like crystals were found to precipitate.

Synthesis of $Li_2(taurine)_2MnCl_4$. Taurine (75 mg, 0.60 mmol) and anhydrous $MnCl_2$ (76 mg, 0.60 mmol) were added to 0.45 mL of a 10 M solution of aqueous LiCl in a 4-mL vial. The mixture was heated to 100 ºC until the precursors were completely dissolved. Then, the vial was left to cool for 2–3 h and square yellow plate-like crystals were found to precipitate.

Synthesis of $(Mg(H_2O)_2)(taurine)_2CuCl_4$. A 4-mL glass scintillation vial was charged with taurine (0.60 mmol, 75 mg) and $CuCl_2$ (0.30 mmol, 40. mg) and 600 µL of 5-M $MgCl_2$ (*aq*). The vial was sealed and heated to 100 °C in a gravity convection oven for 24 h and slowly cooled to room temperature. After three to four days of standing at room temperature, plank shaped crystals of the target compound were formed among powder of the target compound.

Synthesis of $(PEA)_4CuInCl_8$ (PEA^+ = phenethylammonium). Crystals and powders of $(PEA)_4CuInCl_8$ were obtained by combining

stoichiometric quantities of CuCl (17 mg, 0.17 mmol) and In_2O_3 (24 mg, 0.086 mmol) with eight equivalents of phenethylamine (180 µL, 1.4 mmol) in 1 mL of 6-M HCl(*aq*) under a nitrogen atmosphere. A small amount of H_3PO_2 (60 µL, 50 wt. % solution in H_2O) was added to the solution to reduce any trace amount of Cu^{II}.[53] Upon heating to 100 °C, the solids dissolved yielding a light-yellow solution. Quickly cooling the solution while stirring yielded a colorless powder that was collected by filtration, washed with diethyl ether, and dried under reduced pressure for 20 h. Alternatively, slowly cooling the solution at a controlled rate of 4 °C/h yielded colorless plate-like crystals suitable for single-crystal X-ray diffraction.

Synthesis of $(CuCl_2)_4(HIS)_4CuInCl_8$ (HIS^{2+} = histammonium). Crystals of $(CuCl_2)_4(HIS)_4CuInCl_8$ suitable for single crystal X-ray diffraction were prepared by combining CuCl (11 mg, 0.11 mmol), In_2O_3 (16 mg, 0.057 mmol), histamine (53 mg, 0.48 mmol), and H_3PO_2 (35 µL, 50 wt. % solution in H_2O) in 0.4 mL of 12-M HCl (*aq*). The mixture was heated and stirred briefly at 100 °C in a loosely capped vial until all solids dissolved, forming a pale-yellow solution, and then cooled to room temperature. The solution was purged with N_2 for 40 minutes, causing a colorless powder to precipitate. This solid was re-dissolved at 100 °C and then the vial was removed from the heat and allowed to cool. The solution sat at room temperature for four days after which time colorless crystals formed. These crystals were re-dissolved at 100 °C and the solution was slowly cooled to room temperature at a controlled rate of 3 °C/h, forming large chunks of colorless crystalline solid. The solution sat undisturbed at room temperature for six days and was then re-heated to 100 °C to dissolve the previously formed crystals. Additional H_3PO_2 (25 µL, 50 wt. % solution in H_2O) was added and the solution was purged with N_2 for 1 h at room temperature and then for 15 minutes while heating at 100 °C. The solution was slowly cooled to room temperature at 2 °C/h and then allowed to sit undisturbed for four days, resulting in formation of clusters of small colorless blade-like crystals. Note that attempts to synthesize this perovskite following a procedure similar to that outlined above but without the multi-day period between combining the precursors in HCl and the final controlled slow cool yielded crystals of a different phase.

Synthesis of $(PbBr_2)_2(AMTP)_2PbBr_4$ ($AMTP^+$ = 4-(ammoniomethyl)-tetrahydropyran). In a 20-mL glass scintillation vial, $PbBr_2$ (1.0771 g, 2.935 mmol) was dissolved in 3.0 mL of 12-M HBr (*aq*), and 0.236 mL (2.01 mmol) of 4-aminomethyl-tetrahydropyran was added dropwise. The resulting mixture was dissolved with mild sonication. The solution was transferred to a Teflon-capped vapor diffusion chamber with 20 mL of diethyl ether as the antisolvent. The chamber was sealed and left to stand in the dark. After several days, the large colorless plates that formed were isolated by vacuum filtration, washed with diethyl ether and dried under reduced pressure. *Elemental analysis*. Calculated: C 9.65%, H 1.89%, N 1.87%. Found: C 9.76%, H 1.88%, N 2.05%.

Thin films of $(PbBr_2)_2(AMTP)_2PbBr_4$ were prepared by spin casting in a nitrogen-filled glovebox. A circular quartz plate was cleaned by sequential sonications in an aqueous detergent solution, isopropanol, and deionized water. The plate was dried using compressed air and cleaned by UV-ozone. In a nitrogen-filled glovebox, 51.6 mg of the compound were dissolved in 1 ml of DMSO and passed through 0.22 µm PTFE filter. The solution was dropcast onto the substrate mounted in a spin coater then spun at 4000 rpm (4000 rpm/s acceleration) for 60 s under a nitrogen flow. The coated quartz plate was then heated to 100 ºC for 1 minute. Powder X-ray diffraction **(Figure S15)** is consistent with the phase pure recrystallization of $(PbBr_2)_2(AMTP)_2PbBr_4$.

Synthesis of $(Pb_2Cl_2)(CYS)_2PbCl_4$ ($CYS = {}^+H_3N(CH_2)_2S^-$). Aminoethanethiol hydrochloride (140 mg, 12 mmol) and lead(II) acetate trihydrate (230 mg, 6.2 mmol) and lead(II) chloride (170 mg, 6.2 mmol) were added to 30 mL of 6-M aqueous NaCl to form a yellow powder, which upon further stirring turned colorless. The suspension was heated to 100 °C for 10 minutes to afford solid $(Pb_2Cl_2)(CYS)_2PbCl_4$. Single crystals of the target compound may be obtained in low yield by hot-filtration of the product suspension followed by slow-cooling over the course of 12 h. *Elemental analysis*. Calculated: C 4.86%, H 1.43%, N 2.83%, S 6.49%. Found: C 4.66%, H 1.33%, N 2.62%, S 6.29%.

Data Availability. Additional crystallographic information, powder X-ray diffraction data, optical data, and animated structural relationships between intergrowths and parent structures are available in the Supplementary information. Crystallographic information files (CIFs) for the new structures are available from the Cambridge Crystallographic Data Center under reference numbers 1994577–1994579 and 1995031–1995037.

References

34. Stokes, H. T., Hatch, D. M. & Campbell, B. J. ISODISTORT, ISOTROPY software suite. (2020). at <iso.byu.edu>
35. Campbell, B. J., Stokes, H. T., Tanner, D. E. & Hatch, D. M. ISODISPLACE : a web-based tool for exploring structural distortions. *J. Appl. Crystallogr.* **39,** 607–614 (2006).
36. Brese, N. E. & O'Keeffe, M. Bond-valence parameters for solids. *Acta Crystallogr. B* **47,** 192–197 (1991).
37. Slater, J. C. Atomic radii in crystals. *J. Chem. Phys.* **41,** 3199–3204 (1964).
38. Earnshaw, A. & Greenwood, N. N. in *Chemistry of the elements* 367–405 (Elsevier Ltd, 1997).
39. Bruker AXS Inc., *SAINT and SADABS* 8.38A.
40. Sheldrick, G. M. SHELXT – Integrated space-group and crystal-structure determination. *Acta Crystallogr. Sect. A* **71,** 3–8 (2015).
41. Sheldrick, G. M. Crystal structure refinement with SHELXL. *Acta Crystallogr. Sect. C* **71,** 3–8 (2015).
42. Dolomanov, O. V., Bourhis, L. J., Gildea, R. J., Howard, J. A. K. & Puschmann, H. OLEX2: a complete structure solution, refinement and analysis program. *J. Appl. Crystallogr.* **42,** 339–341 (2009).
43. Toby, B. H. & Von Dreele, R. B. GSAS-II: the genesis of a modern open-source all purpose crystallography software package. *J. Appl. Crystallogr.* **46,** 544–549 (2013).
44. Momma, K. & Izumi, F. *VESTA 3* for three-dimensional visualization of crystal, volumetric and morphology data. *J. Appl. Crystallogr.* **44,** 1272–1276 (2011).
45. Hohenberg, P. & Kohn, W. Inhomogeneous electron gas. *Phys. Rev.* **136,** B864–B871 (1964).
46. Perdew, J. P., Burke, K. & Ernzerhof, M. Generalized gradient approximation made simple. *Phys. Rev. Lett.* **77,** 3865–3868 (1996).
47. Giannozzi, P., Baroni, S., Bonini, N., Calandra, M., Car, R., Cavazzoni, C., Ceresoli, D., Chiarotti, G. L., Cococcioni, M., Dabo, I., Dal Corso, A., de Gironcoli, S., Fabris, S., Fratesi, G., Gebauer, R., Gerstmann, U., Gougoussis, C., Kokalj, A., Lazzeri, M., Martin-Samos, L., Marzari, N., Mauri, F., Mazzarello, R., Paolini, S., Pasquarello, A., Paulatto, L., Sbraccia, C., Scandolo, S., Sclauzero, G., Seitsonen, A. P., Smogunov, A., Umari, P. & Wentzcovitch, R. M. QUANTUM ESPRESSO: a modular and open-source software project for quantum simulations of materials. *J. Phys. Condens. Matter* **21,** 395502 (2009).
48. Giannozzi, P., Andreussi, O., Brumme, T., Bunau, O., Buongiorno Nardelli, M., Calandra, M., Car, R., Cavazzoni, C., Ceresoli, D., Cococcioni, M., Colonna, N., Carnimeo, I.,

Dal Corso, A., de Gironcoli, S., Delugas, P., DiStasio, R. A., Ferretti, A., Floris, A., Fratesi, G., Fugallo, G., Gebauer, R., Gerstmann, U., Giustino, F., Gorni, T., Jia, J., Kawamura, M., Ko, H.-Y., Kokalj, A., Küçükbenli, E., Lazzeri, M., Marsili, M., Marzari, N., Mauri, F., Nguyen, N. L., Nguyen, H.-V., Otero-de-la-Roza, A., Paulatto, L., Poncé, S., Rocca, D., Sabatini, R., Santra, B., Schlipf, M., Seitsonen, A. P., Smogunov, A., Timrov, I., Thonhauser, T., Umari, P., Vast, N., Wu, X. & Baroni, S. Advanced capabilities for materials modelling with quantum ESPRESSO. *J. Phys. Condens. Matter* **29,** 465901 (2017).

49. van Setten, M. J., Giantomassi, M., Bousquet, E., Verstraete, M. J., Hamann, D. R., Gonze, X. & Rignanese, G.-M. The PseudoDojo: Training and grading a 85 element optimized norm-conserving pseudopotential table. *Comput. Phys. Commun.* **226,** 39–54 (2018).
50. Deslippe, J., Samsonidze, G., Strubbe, D. A., Jain, M., Cohen, M. L. & Louie, S. G. BerkeleyGW: A massively parallel computer package for the calculation of the quasiparticle and optical properties of materials and nanostructures. *Comput. Phys. Commun.* **183,** 1269–1289 (2012).
51. Del Ben, M., da Jornada, F. H., Canning, A., Wichmann, N., Raman, K., Sasanka, R., Yang, C., Louie, S. G. & Deslippe, J. Large-scale GW calculations on pre-exascale HPC systems. *Comput. Phys. Commun.* **235,** 187–195 (2019).
52. Del Ben, M. D., Yang, C., Li, Z., Jornada, F. H. da, Louie, S. G. & Deslippe, J. Accelerating large-scale excited-state GW calculations on leadership HPC systems. in *SC20 Int. Conf. High Perform. Comput. Netw. Storage Anal.* 1–11 (IEEE, 2020). doi:10.1109/SC41405.2020.00008
53. Connor, B. A., Smaha, R. W., Li, J., Gold-Parker, A., Heyer, A. J., Toney, M. F., Lee, Y. S. & Karunadasa, H. I. Alloying a single and a double perovskite: a $Cu^{+/2+}$ mixed-valence layered halide perovskite with strong optical absorption. *Chem. Sci.* (2021). DOI:10.1039/D1SC01159F
54. Depmeier, V. W. Die Kristallstruktur von Athylammoniumtetrachloromanganat(II) bei Raumtemperatur. *Acta Crystallogr. B* **B32,** 303–305 (1976).
55. Dou, L., Wong, A. B., Yu, Y., Lai, M., Kornienko, N., Eaton, S. W., Fu, A., Bischak, C. G., Ma, J., Ding, T., Ginsberg, N. S., Wang, L.-W., Alivisatos, A. P. & Yang, P. Atomically thin two-dimensional organic-inorganic hybrid perovskites. *Science* **349,** 1518–1521 (2015).

Acknowledgements

This work was funded by the US Department of Energy (DOE), Office of Basic Energy Sciences, Division of Materials Sciences and Engineering, under contract DE-AC02-76SF00515. M.L.A. is supported by an EERE (Office of Energy Efficiency and Renewable Energy) postdoctoral fellowship and B.A.C. is supported by a National Science Foundation (NSF) graduate fellowship (DGE-114747) and the McBain award from Stanford Chemistry. K.P.L. thanks the Center for Molecular Analysis and Design at Stanford University for a graduate fellowship and Stanford Chemistry for the William S. Johnson award. SC-XRD studies were performed either at the Advanced Light Source (beamline 11.3.1) at the Lawrence Berkeley National Laboratory (LBNL) or at Stanford Nano Shared Facilities, supported by the NSF (award ECCS-1542152). We thank Dr. Simon Teat for helpful discussion and Dr. Matthew Smith and Dr. Ethan Crace for experimental assistance. DFT calculations were supported by the US DOE, Office of Basic Energy Sciences, Division of Materials Sciences and Engineering (Theory FWP), under contract No. DE-AC02-05CH11231. We acknowledge computational resources at the Molecular Foundry, supported by the Office of Science, Office of Basic Energy Sciences, of the US DOE under Contract DE-AC02-5CH11231, at the National Energy Research Scientific Computing Center (NERSC; Cori), at the Oak Ridge Leadership Computing Facility (Summit) accessed through the INCITE program (a DOE Office of Science User Facility; grant number DE-AC05-00OR22725), and the Texas Advanced Computing Center (TACC; Stampede 2) through an XSEDE Award (DMR190070) supported by the NSF grant number ACI-1548562.

Author contributions

The authors M.L.A., A.S.V., and B.A.C. synthesized and structurally characterized the materials. M.L.A. and K.P.L. performed the optical measurements. H.I.K. defined and guided the project direction. M.R.F. and J.B.N. conducted the electronic structure calculations and theoretical analyses. All authors helped write the manuscript.

Competing interests

Stanford University has submitted a provisional patent application on this work with H.I.K., M.L.A, and A.S.V. as co-inventors.

Supplementary information

Supplementary information is available at the publication's website:

Correspondence and requests for materials

Correspondence should be addressed to H.I.K.

Extended Data Table 1| Summary of lattice strains estimated for the intergrowth slabs relative to non-intergrown parent structures

Extended Data Table 2| Summary of lattice strains estimated for perovskite slabs relative to non-intergrowth parent structures

Extended Data Table 3| Relative strain tensors for the perovskite slabs

Extended Data Table 4| Relative strain tensors for the intergrowth slabs

EXTENDED DATA FIGURE CAPTIONS

Extended Data Figure 1| The crystal structure of $(RPO(OH)_2)_2CuCl_4$ viewed along the *c*-axis highlighting the hydrogen bond network in the organic bilayer. Carbon bonded hydrogens are not shown for clarity. Each phosphonic acid donates two hydrogen bonds and accepts two hydrogen bonds at the unprotonated oxygen atom. Each phosphonic acid hydrogen bonds only to phosphonic acid groups on the opposing face of the organic bilayer to form the checkerboard pattern illustrated. The elements P, C, H, N, O are colored pink, grey, white, blue, and red, respectively.

Extended Data Figure 2| Schematic illustrating the templating of a hydronium sulfonate between layers of a $CuCl_4^{2-}$ perovskite sublattice. The archetypal parent 3D perovskite with the relevant slice highlighted (a). The parent structure $RbCuCl_3$ is unknown though $RbCuF_3$ is known. The dimensionally reduced product of a copper chloride perovskite as isolated in the single-crystal structure of $(propylammonium)_2CuCl_4$ and the previously reported layered crystal structure of hydronium triflate (b). Structure directing functional groups are highlighted in blue (ammonium) and red (sulfonate). These same interactions are shown in the compound $(H_3O)_2(taurine)_2CuCl_4$. The elements Cu, Cl, C, H, N, S, O, and F are colored dark-green, green, grey, white, blue, yellow, red, and lime-green, respectively.

Extended Data Figure 3| Structural comparison between intergrowths and layered reference structures. The slab for the magnesium intergrowth in $(Mg(H_2O)_2)(taurine)_2CuCl_4$ (a) and the reference structure $KMg(H_{0.5}SO_4)_2{\bullet}2(H_2O)$ (b). The slab for the lithium intergrowth in $Li_2(taurine)_2CuCl_4$ (c) and the reference structure α-$Li(NH_4)SO_4$ (d). Mg, Li, S, O, H atoms are shown as green, light blue, yellow, red, and white spheres, respectively.

Extended Data Figure 4| Schematic illustrating the templating of a heterostructure with $CuInCl_8$ double perovskite layers and anionic chains of $CuCl_2^{1-}$. (a) The parent layered structure $(PEA)_4CuInCl_8$ and 1D chain structure $(phthalazinium)CuCl_2$ crystallize with structure directing hydrogen bonds between the organic molecules and the inorganic sublattices highlighted in blue and yellow, respectively. (b) The corresponding interactions are highlighted in the templated layered heterostructure $(CuCl_2)_4(HIS)_4CuInCl_8$. Cu, In, Cl, C, and N atoms are colored gold, light-grey, lime-green, grey, and blue, respectively. Some H atoms are omitted for clarity.

Extended Data Figure 5| Schematic illustrating the templating of heterostructures containing layered lead-halide perovskites and layers derived from (001) slices of the PbX_2 (X = Cl, Br) structure-type. The parent 3D inorganic structures with relevant slices highlighted (a) and their dimensionally reduced progeny (b). Note dimensionally reduced (001) slices of PbX_2 have not be isolated outside of the layered heterostructures reported here. Structure directing alkylammonium groups are highlighted in blue and substitution sites for the coordinating ether and sulfide groups in the heterostructures are highlighted in yellow. The location of these same templating groups and substitution sites are highlighted in the templated layered heterostructures $(PbBr_2)_2(AMTP)_2PbBr_4$ and $(Pb_2Cl_2)(CYS)_2PbCl_4$ (c). Pb, Cl, Br, C, N, O, S atoms are colored light-blue, green, orange, grey, blue, red, and yellow, respectively. H atoms are omitted for clarity.

Extended Data Figure 6| Structural comparison between intergrowths and slices of the 3D reference structure. Face-on comparisons of the (001) slab of $PbCl_2$ (left)—which is isostructural to that of $PbBr_2$—to the intergrowth sublattices in $(Pb_2Cl_2)(CYS)_2PbCl_4$ (center) and $(PbBr_2)_2(AMTP)_2PbBr_4$ (right). Lead, chlorine, sulfur, bromine and oxygen atoms are shown as light blue, green, yellow, orange, and red spheres, respectively.

Extend Data Figure 7| Comparison between the crystal structure of $(Pb_2Cl_2)(CYS)_2PbCl_4$ (a) and the structural model used for calculation of absorption spectra and electron-hole interactions with half the unit-cell volume (b). Disordered atoms in (a) are resolved and hydrogen atoms in (b) are removed for clarity. Both structures are viewed along the *c*-axis. Unit-cell borders are shown in red. The atom colors are light blue (Pb), green (Cl), grey (C), blue (N), and yellow (S).

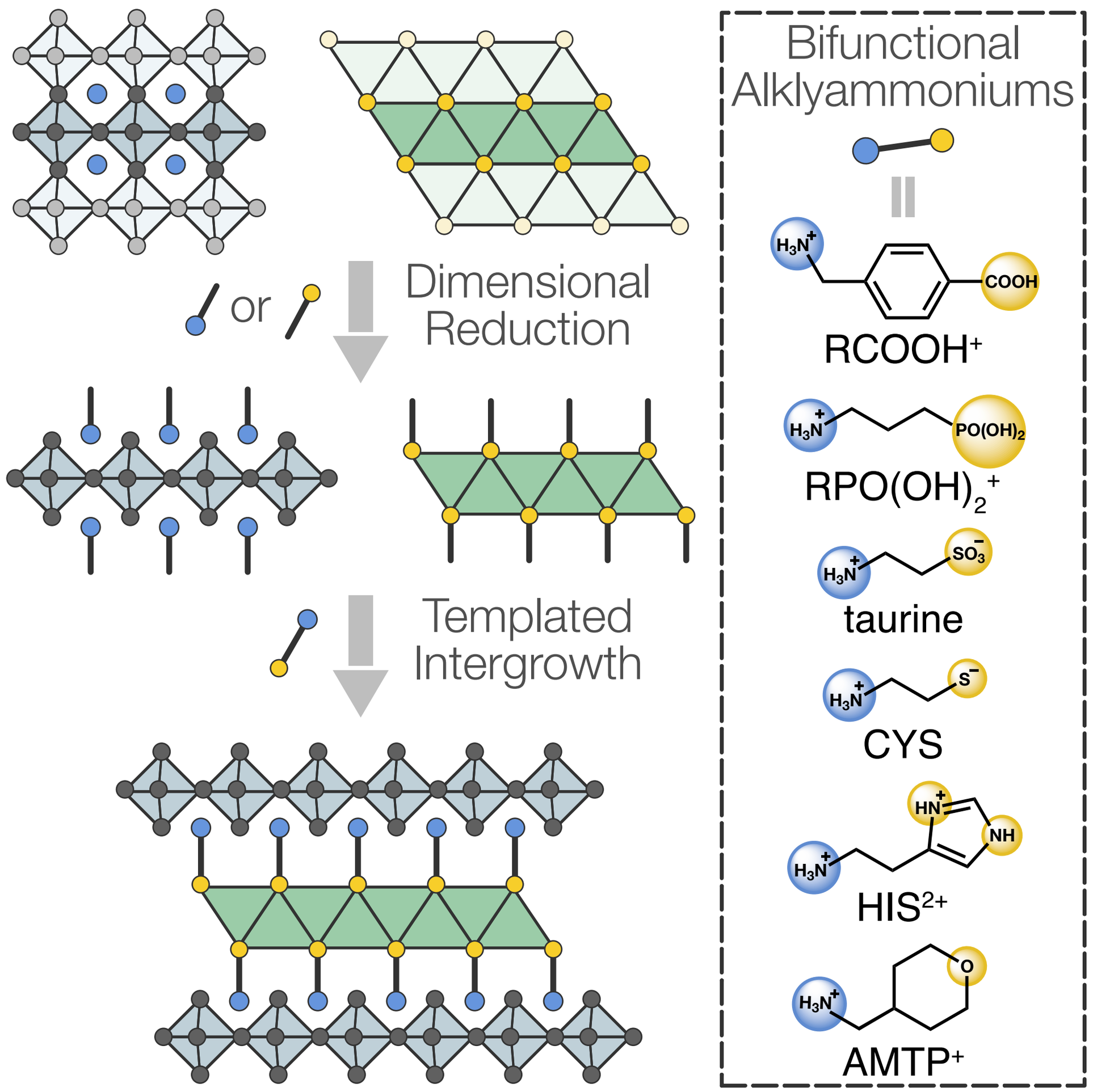
Bifunctional
Alklyammoniums
or
Dimensional
Reduction
Templated
Intergrowth
RCOOH+
RPO(OH)2+
taurine
CYS
HIS2+
AMTP+

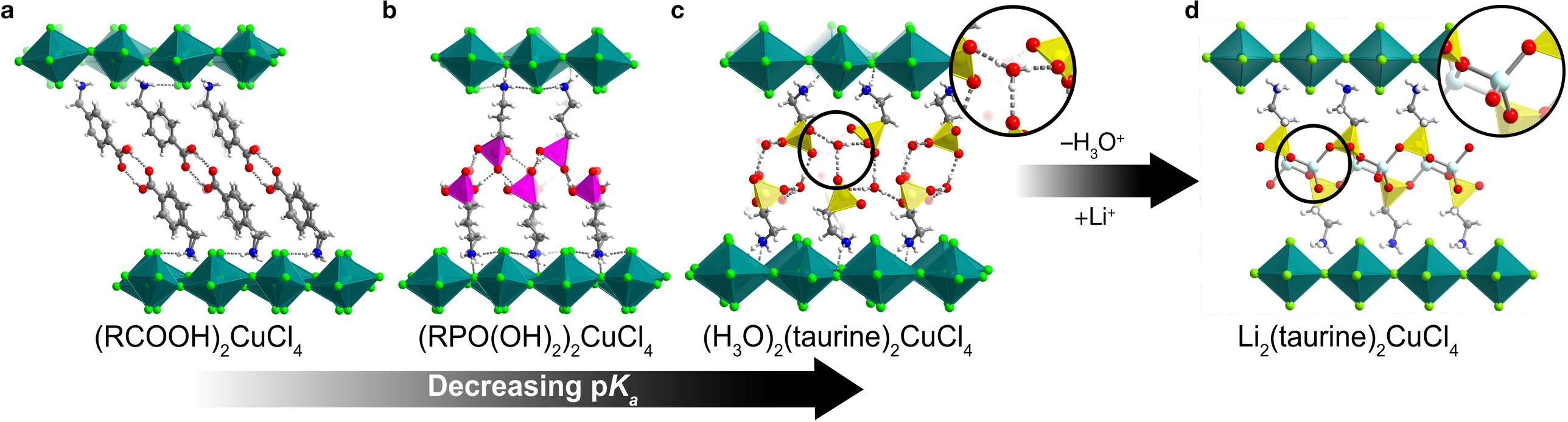
a
b
c
d
$(RCOOH)_2CuCl_4$
$(RPO(OH)_2)_2CuCl_4$
$(H_3O)_2(taurine)_2CuCl_4$
$Li_2(taurine)_2CuCl_4$
$-H_3O^+$
$+Li^+$
Decreasing pK_a

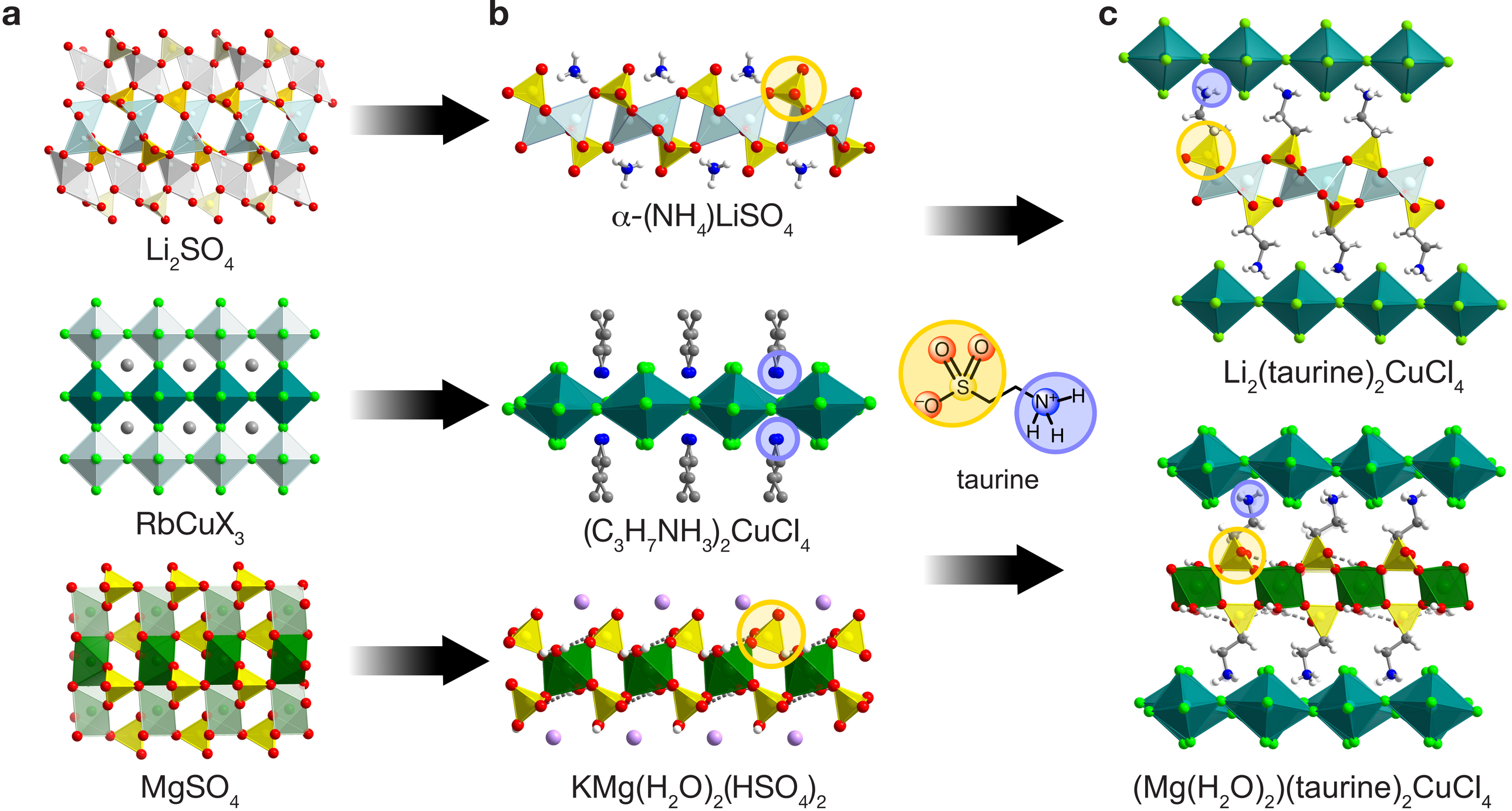
a
b
c
Li_2SO_4
α-$(NH_4)LiSO_4$
$Li_2(taurine)_2CuCl_4$
$RbCuX_3$
$(C_3H_7NH_3)_2CuCl_4$
taurine
$MgSO_4$
$KMg(H_2O)_2(HSO_4)_2$
$(Mg(H_2O)_2)(taurine)_2CuCl_4$

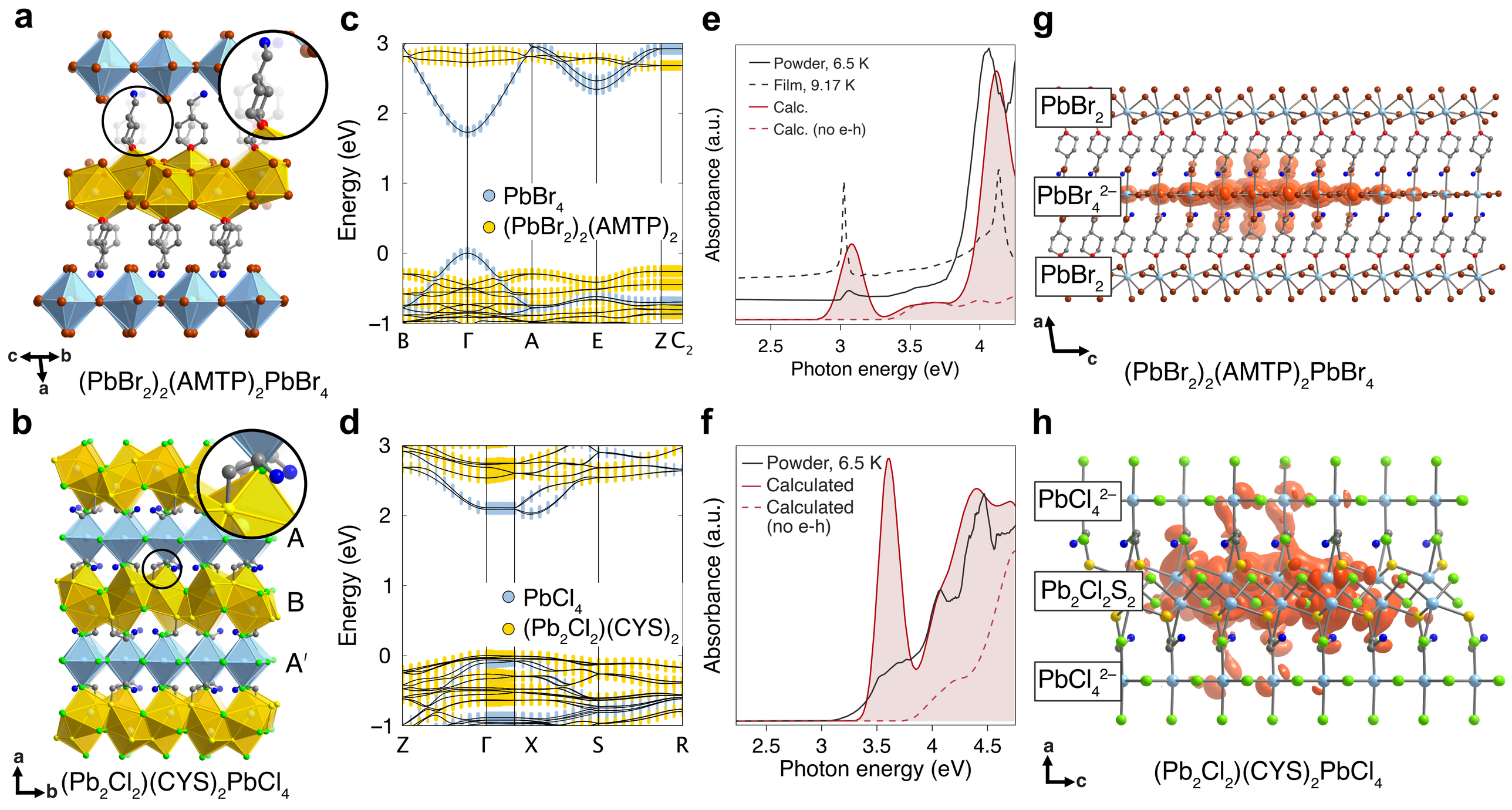
a
c
b
a
(PbBr2)2(AMTP)2PbBr4
b
A
B
A′
a
b
(Pb2Cl2)(CYS)2PbCl4
c
Energy (eV)
3
2
1
0
−1
B
Γ
A
E
Z
C2
PbBr4
(PbBr2)2(AMTP)2
d
Energy (eV)
3
2
1
0
−1
Z
Γ
X
S
R
PbCl4
(Pb2Cl2)(CYS)2
e
Absorbance (a.u.)
Powder, 6.5 K
Film, 9.17 K
Calc.
Calc. (no e-h)
2.5
3
3.5
4
Photon energy (eV)
f
Absorbance (a.u.)
Powder, 6.5 K
Calculated
Calculated
(no e-h)
2.5
3
3.5
4
4.5
Photon energy (eV)
g
PbBr2
PbBr4 2−
PbBr2
a
c
(PbBr2)2(AMTP)2PbBr4
h
PbCl4 2−
Pb2Cl2S2
PbCl4 2−
a
c
(Pb2Cl2)(CYS)2PbCl4